Post-Print of an Accepted Manuscript on the Laboratory of Turbulent Flows Website

Complete citation:

Wang, S., & Ghaemi, S. (2019). Effect of vane sweep angle on vortex generator wake. *Experiments in Fluids*, *60*(1), 1-16. doi: 10.1007/s00348-018-2666-1

The final publication is available at https://doi.org/10.1007/s00348-018-2666-1

The Accepted Manuscript begins on the next page.

Effect of Vane Sweep Angle on Vortex Generator Wake

Sen Wang[1] · Sina Ghaemi[1]

Abstract

The effect of varying the sweep angle of the vane of different vortex generators (VGs) on the statistics of the wake flow and the coherent structures was investigated. Pairs of rectangular, trapezoid, and delta vanes with sweep angle varying in ascending order were arranged an equal but opposite angle with respect to the flow. A single rectangular vane was also investigated to identify the effect of vane pairing. The VGs were installed in the thin laminar boundary layer of a flat plate at Reynolds number of 930, based on VG height and free-stream velocity. Time-resolved tomographic particle image velocimetry (tomo-PIV) was carried out in a volume covering the wake, and stereo-PIV was used to characterize the wake at two cross-flow planes. The measurements showed two counter-rotating streamwise vortices, which induce a strong upward motion along the centerline of the wake. A pair of secondary counter-rotating streamwise vortices were also observed. The single rectangular vane showed a primary streamwise vortex and a weaker secondary streamwise vortex with opposite rotation. The rectangular VG produced the strongest streamwise vortices, wall-normal motion, and mean vorticity fluctuation. The evaluation of the vertical flow transport along the center of wake shows that the paired VG has a significant effect on enhancing the wall-normal flow motion. The investigation of the instantaneous coherent structures and proper-orthogonal-decomposition (POD) of the three-dimensional velocity fluctuations indicated that the coherence and strength of the vortices were inversely proportional to the sweep angle of the VG. The delta vane VG, with the largest sweep angle, produced more small-scale turbulence while the rectangular VG, with an upswept vane, produced the most coherent streamwise vortices. The investigation of the rate of momentum transport shows that the RVG has the best performance in improving flow mixing, followed by the TVG, single RVG, and DVG. When evaluating the performance of VG with respect to the ratio of mixing enhancement over drag, the TVG is proved to be the most efficient device. It confirms the possibility of lowering the device drag while maintaining the effectiveness of VG by varying the sweep angle. However, the performance of DVG is shown to be around 60% of the TVG, which suggests that over increasing the sweep angle has an adverse effect on the VG efficiency.

Abbreviations

c	=	vortex generator chord (mm)	U	=	instantaneous streamwise velocity (m/s)
h	=	vortex generator height (mm)	U_∞	=	free-stream velocity (m/s)
f	=	focal length of camera lens	V	=	instantaneous wall-normal velocity (m/s)
u	=	streamwise fluctuating velocity (m/s)	W	=	instantaneous spanwise velocity (m/s)
v	=	wall-normal fluctuating velocity (m/s)	β	=	incidence angle of the vane (deg)
x	=	streamwise direction	γ	=	leading-edge sweep angle (deg)
y	=	wall-normal direction	δ	=	boundary layer thickness (mm)
z	=	spanwise direction	ω_x	=	streamwise vorticity fluctuation (s^{-1})
C_D	=	coefficient of drag	ω_z	=	spanwise vorticity fluctuation (s^{-1})
P	=	turbulence production (m^2/s^3)	Ω_x	=	streamwise mean vorticity (s^{-1})
Q	=	Q-criterion (s^{-2})			

✉ Sina Ghaemi
ghaemi@ualberta.ca

[1] Department of Mechanical Engineering, University of Alberta, Alberta, Canada

1 Introduction

Vortex generator (VG) is a passive flow control device that has been applied to various aerodynamic systems to improve their performance. VGs are applied to delay flow separation or accelerate the reattachment process. As a result, VGs can increase lift and stall angle-of-attack of an airfoil, and reduce the drag caused by flow separation. One of the early VGs was introduced by Taylor (1947) by a row of inclined metal vanes installed on a surface. The height (h) of the vanes was about the boundary layer thickness (δ) and they were inclined with respect to the streamwise direction.

The flow control mechanism of VG was studied by Schubauer and Spangenberg (1960) through investigation of several VGs under adverse pressure gradient. They showed that VGs transfer momentum between the high speed free-stream and the low-speed near wall flow. The investigations of Lin et al. (1990; 1999) showed that vane-type VGs are capable of accomplishing a large transport of momentum by generating streamwise vortices. The streamwise vortices eject the low momentum flow away from the wall, and transfer high momentum flow towards the wall. This adds to the kinetic energy of the boundary layer to relax the adverse pressure gradient, and prevent/delay flow separation.

A disadvantage of large, conventional, vane-type VGs is their large parasite drag. The streamwise vortices produced by conventional VGs may dominate the flow field even after the flow has reattached (Lin 1999). To compensate for the parasitic drag force, low-profile VG was introduced by Kuethe (1972). A wavy surface with protrusions of semi-circular cross-section and chamfered ends was placed inclined at 15º with respect to the flow. The wavy protrusions had a height to boundary layer thickness ratio of δ/h = 0.27 to 0.42. This low-profile VG produced quasi-streamwise vortices, which suppressed the formation of the Kármán vortex street. As a result, acoustic noise was reduced, and velocity deficit was recovered faster. The effectiveness of low-profile VGs has also been confirmed by Lin (1999) over a backward facing ramp using oil-flow visualization. It was shown that, in terms of delaying the separation and reducing reattachment distance, the vane-type VGs with small $h/\delta \sim 0.2$ and large $h/\delta \sim 0.8$ have performed similarly. The generated streamwise vortices of the $h/\delta \sim 0.2$ VG also did not disturb the far downstream flow. Therefore, low-profile VGs can provide enough flow mixing to prevent/delay separation with lower drag penalty.

The experiments of Lin (1990; 1991; 1999) examined the effectiveness of various VGs over a two-dimensional backward-facing ramp under adverse pressure gradient. Their oil visualization revealed that the efficient VGs have one characteristic in common: they generate pairs of counter-rotating streamwise vortices (Lin 1999). Although further improvement of the performance is feasible by optimizing geometric parameters such as VG height, chord length, incidence angle, and spacing between the vanes (Rao and Kariya 1988).

As it was discussed, adjusting the device height allows a compromise between the parasitic drag of the VG and its flow control effectiveness. The local flow velocity at the tip of a VG with optimum height of $h/\delta \sim 0.2$ should be about 75% of the free-stream velocity (Lin 1999). Additional increase of the VG height significantly increases its drag, while lowering h/δ below 0.1 reduces the effectiveness of the VG for separation control (Lin 1999). Another important geometric dimension affecting the flow control effectiveness is the incidence angle (β) between VG vane-blades and the streamwise flow direction (see Fig. 1). It has been generally observed that VGs with larger incidence angles produce stronger streamwise vortices (Pauley and Eaton 1994). Godard and Stanislas (2006) investigated the effect of β of delta-shaped vanes arranged to generate co-rotating and counter rotating streamwise vortices. Their particle image velocimetry (PIV) measurements showed that the optimum incidence angle is about 18 deg.

The gap between the VG vanes affects the interaction between the counter-rotating streamwise vortices. Pauley and Eaton (1994) observed that the counter-rotating streamwise vortices decay faster when they are closer, due to the mutual cancellation of the vortices. Betterton et al. (2000) performed measurements using laser Doppler anemometry, and found that counter-rotating vortices produced by vane-type VGs with a gap of 1h decayed slower than vane VGs with no gap. The numerical study conducted by Froster and White (2014) and the experimental investigation by Lin (1999) also showed that the strength of the generated vortices is proportional to the chord length.

A remaining geometric parameter, to optimize the performance of the VG, is the shape of the VG vane. Delta, trapezoidal, and rectangular vanes with different leading-edge sweep angles have been applied in the past literature (e.g., Lin et al. 1994; 1999; Holmes et al. 1987; Sun 2015). However, to the authors' knowledge, there has not been any systematic investigation of the effect of vane shape on the performance of VGs or transport of momentum.

The current study was conducted to investigate the effect of the shape of the VG vane on the three-dimensional organization of the wake flow. State-of-

the-art high-speed tomographic PIV (tomo-PIV) system was applied to provide time-resolved three-dimensional measurement of wake evolution, vortical structures, and turbulence statistics in the near wake region. Three pairs of vanes with rectangular, delta, and trapezoidal shapes arranged in a symmetric configuration were placed in a laminar boundary layer. A single vane configuration was also investigated to characterize the interaction between vortices.

2 Experimental setup

2.1 Flow facility

The experiments were conducted in a 10 m long water-flume with rectangular cross-section. The test-section was 75 cm wide with a water height of 50 cm. The free-stream velocity was $U_\infty = 0.155$ m/s, and the Reynolds number was 930, based on the VG height and free-stream velocity. The VGs were installed 65 mm downstream of the leading edge of a flat plate. The flat plate had a half-wedge leading edge and was installed vertically at zero angle-of-attack. In the absence of the VG, the boundary layer was laminar with a thickness of 3 mm, and shape factor of 2.7 at the location of the VG. This was estimated from preliminary planar PIV measurements.

2.2 Vortex generators

The investigated VGs include a delta VG (DVG), a trapezoidal VG (TVG), and a rectangular VG (RVG) as demonstrated in Fig. 1a, 1b, and 1c, respectively. The DVG has the largest leading-edge sweep angle (γ) while RVG has zero sweep angle ($\gamma = 0$). A single RVG is also investigated as shown in Fig. 1d. The coordinate system is located at the trailing edge of VG. The geometric parameters such as height (h), chord length (c), and incidence angle (β) are defined in Fig. 1b. These geometric parameters effect the performance of VGs, as discussed in the Introduction. Therefore, to study the effect of vane shape, the other parameters are kept the same for all the investigated VGs, as listed in Table 1. The VG models are 3D printed (Form 2, Formlabs) using transparent resin to reduce the laser reflection during the tomo-PIV experiment. The printer has a laser spot size of 140 µm, and a layer height of 25-100 µm. The minimum wall thickness of the VGs is around 1.7 mm, which is higher than the minimum unsupported wall thickness of the 3D printer (0.6mm). The printing material has less than 1% gain of weight when immersed in water for 24 hours. During the experiment, the VGs were in water only for the PIV recording (~few hours). No obvious shape deformation was detected after the experiments.

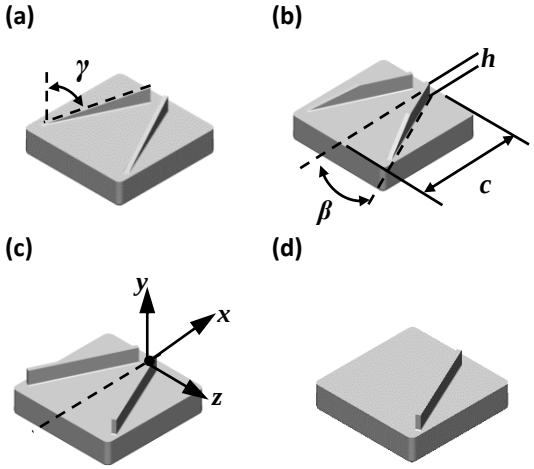

Fig. 1 3D model of the VGs with (a) delta, (b) trapezoidal, and (c) rectangular vanes. (d) A single rectangular vane for comparison with the pair configuration. These VGs are referred to as DVG, TVG, RVG and single RVG, respectively.

Table 1 The common dimensions of the VGs

Height (h), mm	Chord length (c), mm	Incidence angle (β), deg
6.0	36.0	25.0

2.3 Stereoscopic particle image velocimetry

Stereoscopic particle image velocimetry (stereo-PIV) measurement was conducted to measure the mean velocity fields in y-z plane across the wake for drag estimation. As shown in Fig. 2, the stereo-PIV setup consisted of two Image Intense (LaVision GmbH) CCD cameras with a solid viewing angle of about 100 deg. Scheimpflug adapters were installed on the glass wall of the flume to improve image quality. A detail view of the VG and the coordinate system is also given in Fig. 2 (from left to right). The measurement was carried out at $x = 5h$ within a field-of-view with dimensions of 35 × 41 mm^2 (5.83h × 6.83h) at digital resolution of 29.4 µm/pix. The cameras were equipped with Nikon lenses with f = 105 mm at an aperture setting of f /11, which provides depth-of-focus of approximately 8 mm. An Nd:YAG laser (Gemini, NewWave Research) was used to form a 2 mm thick laser sheet. This relatively thick laser sheet accommodates the large out-of-plane motion of the particles while capturing their smaller in-plane motion in the y and z directions. Silver-coated 2 µm spherical glass beads (SG02S40 Potters Industries) with density of 3.6 g/cm^3 were used as

tracers. A two-dimensional glass sheet with a printed grid of black circles was used for camera calibration. The target was imaged at three x locations, including the center of the laser sheet and with ± 0.5 mm offset in streamwise direction. The calibration image was mapped using a third order polynomial in Davis 7.4 (LaVision GmbH). For each VG, a set of 1,500 images was collected at 5 Hz with a laser pulse interval of 1000 μs. The self-calibration was conducted following Wieneke (2005) in Davis 8.3 (LaVision GmbH). The final root-mean-square (RMS) of the calibration polynomial fit was 0.74 pixels. The signal-to-noise ratio (SNR) of the images was improved by subtracting the minimum intensity of the ensemble of images from each image and normalizing the images using the ensemble average. Vector fields were calculated with stereoscopic cross-correlation using multi-pass algorithm with a final interrogation window of 32 × 32 pixel (0.94 × 0.94 mm^2) at 75% overlap (Davis 8.3, LaVision GmbH). Images were post-processed to remove spurious vectors using universal outlier detection (Westerweel and Scarano 2005).

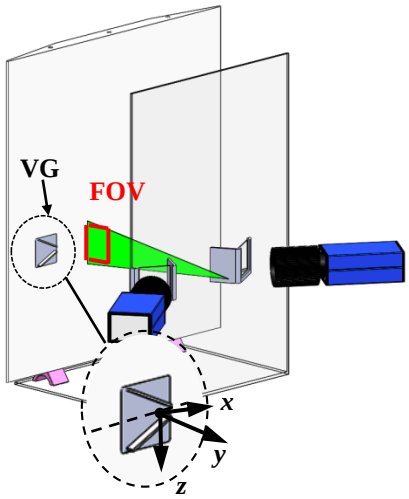

Fig. 2 The relative location of the cameras, laser sheet, VG, and the flat plate in stereo-PIV measurement. The field-of-view is labeled as FOV downstream of the VG.

2.4 Tomographic particle image velocimetry

The wake of the VG was measured using time-resolved tomo-PIV. The imaging system consisted of four high speed cameras (v611 phantom), equipped with Nikon lenses with f = 105 mm focal length. The aperture size was f /16, which provide 13 mm depth-of-field. Sheimpflug adapters were employed to align the focus plane of the imaging system and the measurement plane. The sensor of the camera had 1280 × 800 pixels, each 20 × 20 μm^2. The relative location of the imaging system, VG, and the illuminated volume is shown in Fig. 3. The left camera (L) and right camera (R) had a solid viewing angle about 60 deg, while the angle between the top (T) and bottom (B) cameras was around 40 deg. Since the left and right cameras were imaging the region of interest at a shallow angle relative to the channel wall, glass prisms were installed on the flume wall to improve focusing and reduce astigmatism.

The illuminating source was a dual-head Nd:YLF (Photonics Industries, DM20-527DH) with 20 mJ per pulse at 1 kHz. The laser sheet was collimated and cropped using knife edges to obtain a top-hat intensity laser profile with cross-section of 92×13 mm^3 (15h × 2.5h) in x and y direction, respectively. A 2 mm gap was kept between the laser sheet and the flat plate to reduce laser reflection from the wall and cover the wake as it expands. The measurement volume was 92×55×13 mm^3 (15h × 9h × 2.5h) at digital resolution of 64.9 μm/pix (magnification of 0.3). The seeding particles were hollow glass spheres (~20 μm) with a density of approximately 1.10 g/cc (110P8, Potters Industries LLC). The seeding density was 0.02 particles per pixel (ppp). The particle size was visually estimated from the images to be around 2-4 pixels. Single-frame images were acquired at a recording rate of 800 Hz (Δt = 1.25 ms). Target calibration was conducted using a 3D calibration target (type 11, LaVision GmbH), and the mapping was performed using a third-order polynomial function. The self-calibration procedure was applied to reduce the image distortion and improve the residual of the disparity map from 1-3 pixels to 0.03 pixels as suggested by Wieneke (2008). The SNR was improved by subtracting the minimum intensity of all the images from each image, and normalizing using the ensemble average. The images were also improved by subtracting the local minimum and normalizing using the local average over a kernel of 100 pixels. Volumetric reconstruction of the light intensity was performed using an accelerated MART algorithm (Elsinga et al. 2006) in DaVis 8.4 (LaVision, GmbH). The reconstructed image has a volume of 1421 × 848 × 324 pixel. Volumetric correlation of the 3D reconstructed images was carried out using volume deformation iterative multi-grid technique (VODIM), developed by Scarano and Poelma (2009). For each vector field, sliding-average correlation of three successive pairs of images (Δt = 3 × 1.25 ms) was applied to reduce the correlation noise. A total of 3,500 images were processed for each VG using three iterations with interrogation volumes of 32 × 32 × 32 voxel (2.08 × 2.08 × 2.08 mm^3) and 75% overlap.

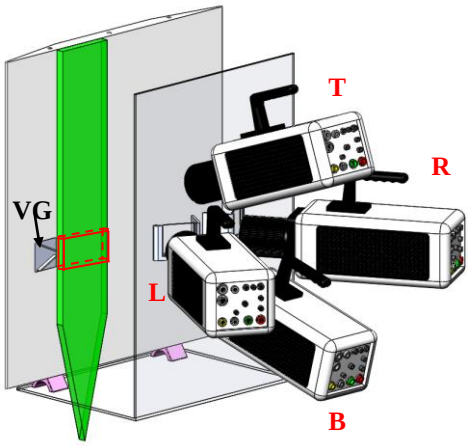

Fig. 3 A schematic of the tomo-PIV imaging system, water-filled prisms, illuminated volume, VG and the flat plate. The solid-viewing angle between the top camera (T) and bottom camera (B) was ~40°. The viewing angle between the left (L) and right (R) cameras was ~60 deg.

3 Result

The mean flow, vorticity field, turbulence production, and dominant coherent structures in the wake of the four VGs are investigated in this section. The subscript of a variable represents its direction, and the < > symbol indicates that the variable is averaged in time.

3.1 Mean flow field

3.1.1 Wake development

The mean streamwise and wall-normal velocities are normalized with the free stream velocity U_∞, and their iso-surfaces are presented in Fig. 4 for the four VG configurations. The $0.9U_\infty$ iso-surfaces are rendered in transparent yellow to reveal the boundaries of the 3D wake. The blue iso-surface is the region of negative wall-normal velocity ($-0.1U_\infty$), and the green region represents the positive wall-normal velocity ($+0.1U_\infty$). Due to the limitation of the measurement volume in the wall-normal direction, top of the iso-surfaces is cropped at y =2.5h. Therefore, the start of the cropped isosurface indicates that the boundaries of the wake has expanded up to y=2.5h. In Fig. 4a, the cropping of the $0.9U_\infty$ iso-surface happens at x = 6h downstream the DVG. The same cropping occurs at x = 4h and x = 3h for the TVG and the RVG in Fig. 4b and 4c respectively. The observation indicates that RVG has the largest wake in the wall-normal direction, followed by the TVG, and DVG. This means that the velocity deficit behind RVG covers a larger volume, while the velocity deficit of DVG is focused in a smaller region. The wake of the single RVG in Fig. 4d is smaller in the wall-normal direction with respect to its pair counter-part (RVG) as seen by the location of the cropped iso-surface.

The iso-surfaces of wall-normal velocity indicate momentum transport between the free-stream and the near-wall region. In the wake of the DVG, two small blue iso-surfaces of downward motion are observed along the sides of a larger upward motion at the wake centerline. The TVG produces a stronger wall-normal velocity than the DVG, and the downward velocity iso-surfaces is present across the entire streamwise range. However, the RVG shows the largest upward and downward velocity iso-surfaces, as an indication of the strongest wall-normal mixing. The single RVG has equivalent upward and downward velocity iso-surfaces. The difference between the pair and the single RVG demonstrates that the counter-rotating vortices intensify the transport of upward flow by inducing a focused motion. The wake of the single RVG in Fig. 1d is inclined with respect to the x axis and gradually moves away from the trailing edge of the VG.

A pair of streamwise vortices is expected to be present between iso-surfaces of positive and negative wall-normal velocity. The results in Fig. 4 show that the gap between the vortex cores, and the width of the wake, increases as the sweep angle of the vane leading edge (γ) decreases. The RVG with γ = 0 has the largest distance between the counter-rotating vortices (i.e. wider wake). On the other hand, the DVG has the smallest distance between the vortices and the largest γ. The smaller γ results in earlier formation of the streamwise vortices along the edge of the VG vane, and therefore a wider wake. The smaller γ also corresponds to a larger frontal area of the VG. Integration of the velocity deficit is required to confirm if a wider wake is associated with a larger drag. However, it was confirmed here that smaller γ increases the wall-normal momentum transport in a wider wake.

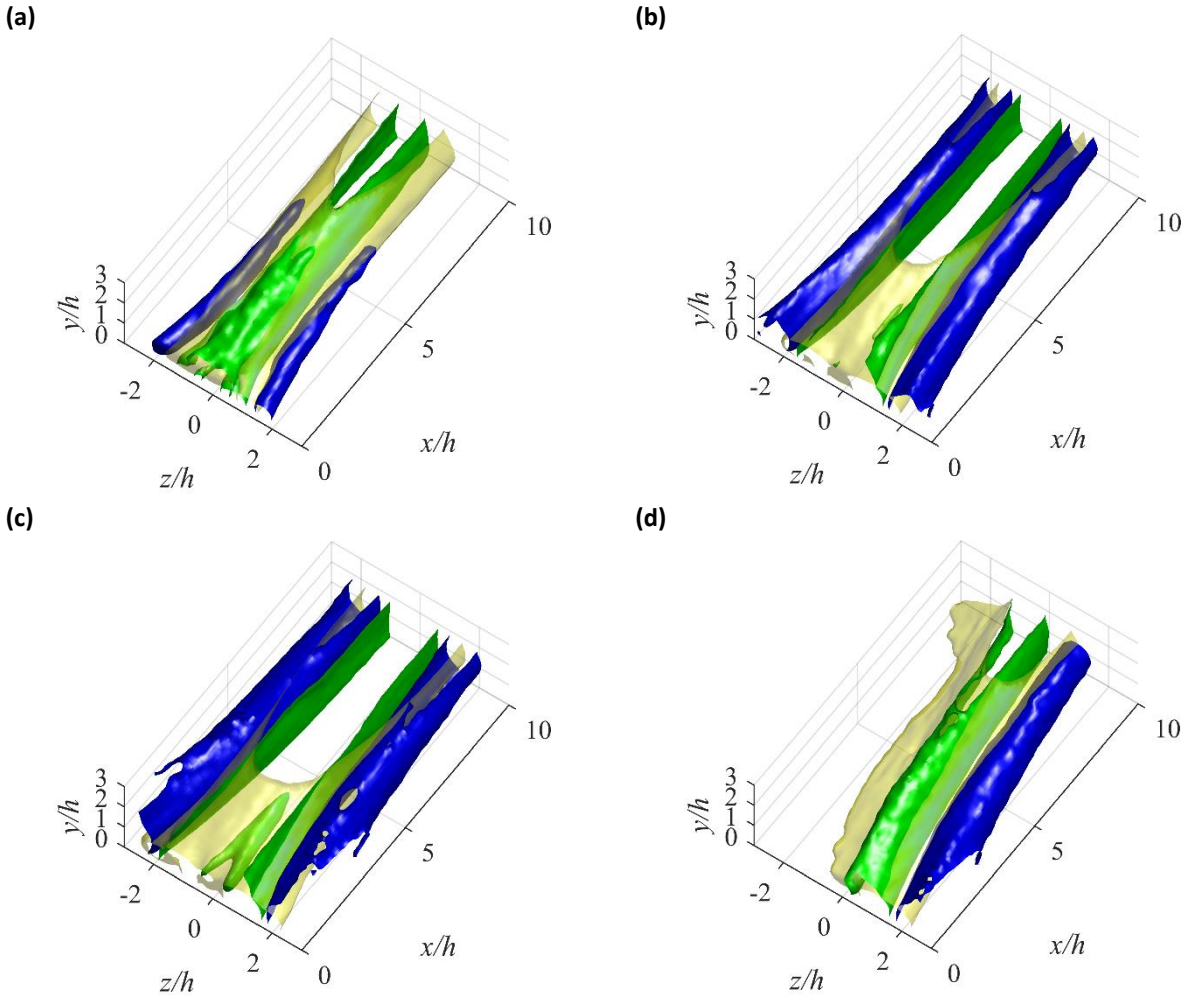

Fig. 4 Iso-surfaces of mean velocity in the wake of a pair of (a) DVG, (b) TVG, (c) RVG, and (d) the single RVG. The transparent yellow shows iso-surface of mean streamwise velocity with $\langle U \rangle = 0.9U_\infty$. The green and blue iso-surfaces show mean wall-normal velocity at $\langle V \rangle = +0.1U_\infty$ and $-0.1U_\infty$, respectively.

The velocity deficit of the wake is further investigated by plotting the mean streamwise velocity at three different levels in Fig. 5. Transparent yellow, transparent green, and solid blue are used to indicate iso-surfaces of $0.7U_\infty$, $0.6U_\infty$, $0.5U_\infty$, respectively. As seen in Fig. 5a, DVG has the smallest wake deficit and fastest velocity recovery. The $0.5U_\infty$ iso-surfaces last till $x \approx 4h$, and the $0.6U_\infty$ iso-surfaces last till $x \approx 6h$. In the wake of the TVG, the $0.5U_\infty$ iso-surfaces last much longer, such that they can still be observed at $x = 8h$. Also, the $0.6U_\infty$ iso-surfaces are detected through the entire measured streamwise range. The RVG also has a larger wake deficit compared with the DVG. The $0.5U_\infty$ iso-surfaces are observed at the vortex core of the primary and secondary vortices close to the trailing edge of VGs. The $0.5U_\infty$ iso-surface of the primary vortices lasts till $x \approx 4h$, while the $0.5U_\infty$ region of the secondary vortices only lasts only about $1h$ in streamwise direction. The $0.6U_\infty$ iso-surfaces are detected through the entire domain.

Therefore, DVG has the smallest wake deficit. TVG shows a slower recovery of wake deficit than the RVG, due to its weaker wall-normal mixing. The contour of Fig. 5d indicates that the single RVG has a faster recovery rate with respect to the pair of RVG. The single RVG also does not have the secondary deficit zones of the paired configuration observed in Fig. 5c.

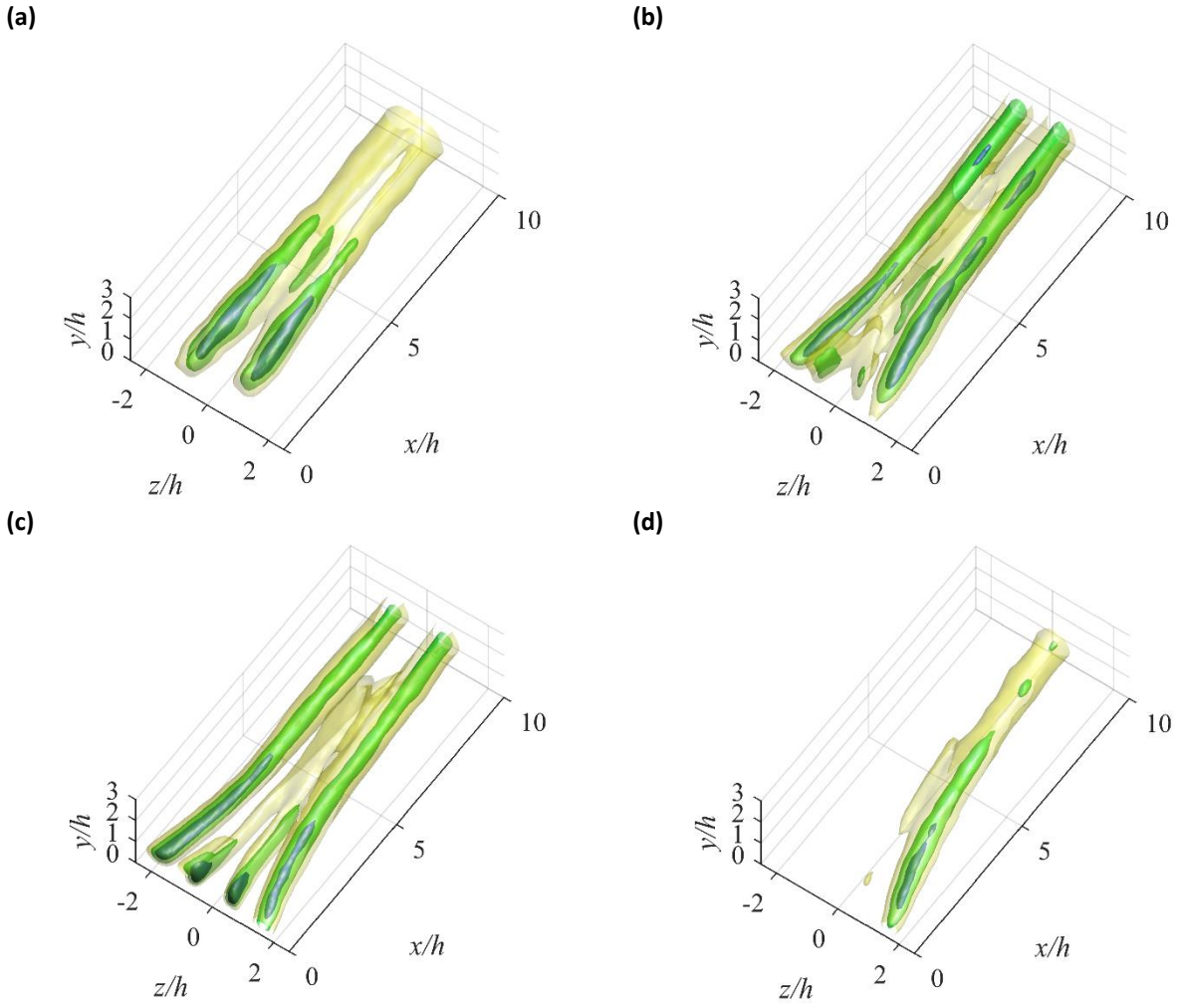

Fig. 5 Iso-surfaces of mean streamwise velocity in the wake of (a) the DVG, (b) the TVG, (c) the RVG, and (d) the single RVG. The iso-surface colored with transparent yellow, transparent green, and solid blue represent mean streamwise velocity at $\langle U \rangle = 0.7U_\infty$, $\langle U \rangle = 0.6U_\infty$, and $\langle U \rangle = 0.5U_\infty$, respectively.

To study the effect of γ on the flow pattern, the distance between vortex cores (d_c) and the width of wake (d_w) against x are plotted in Figs. 6a and 6b, respectively. The estimation of d_c is conducted by measuring the distance between the iso-surfaces of low-speed $\langle U \rangle$ from Fig. 5, and d_W is characterized by the width of $0.9U_\infty$ from Fig. 4. The single RVG is excluded from this comparison since its wake is asymmetric and has a single vortex core. The result shows that the RVG (γ = 0 deg) has the largest d_c across x, followed by the TVG (γ = 73 deg) and DVG (γ = 81 deg). As seen in Fig. 6a, d_c is reduced and the vortices are closer with increase of γ. It is also observed that d_c is large close to the trailing edge, becomes smaller with increase of distance from the trailing edge, and eventually tends toward an asymptote. This shows that the streamwise vortices converge towards the wake centerline (z = 0) and eventually become parallel. A similar trend is also observed in Fig. 6b, such that d_w decreases with increase of x. The DVG, with the highest γ, has the widest wake, followed by TVG and RVG. At $x = 1h$, d_w for TVG and DVG is ~15% and ~30% smaller than RVG, respectively. The wake significantly narrows in the near wake region while it maintains a constant width at $x > 4h$ for all the VGs.

The effect of d_c on wall-normal flow motion along the wake centerline (z = 0) is investigated by calculating the mean vertical transport (VT) defined as

$$\mathrm{VT} = \frac{1}{U_\infty} \int_{0.3h}^{2.5h} \langle V \rangle \mathrm{d}y. \quad (1)$$

The centerline is selected for this integration since it indicates the interaction of counter-rotating vortices and contains the peak of positive $\langle V \rangle$. The plot of VT against x in Fig. 7 shows that the DVG and single RVG induce a similar magnitude of vertical motion,

which grows from ~0.16 to 0.37 with increase of x. The VT of the RVG and TVG increases from ~0.32 to 0.68 along the centerline. For all the VGs, a similar trend of increase in wall-normal motion with x is observed, which reaches a relatively constant value at $x>6h$. The increase in VT is associated with reduction in the distance of the streamwise vortices as observed in Fig. 6a; the fluid ejection away from the wall becomes stronger as the vortices converge.

(a)

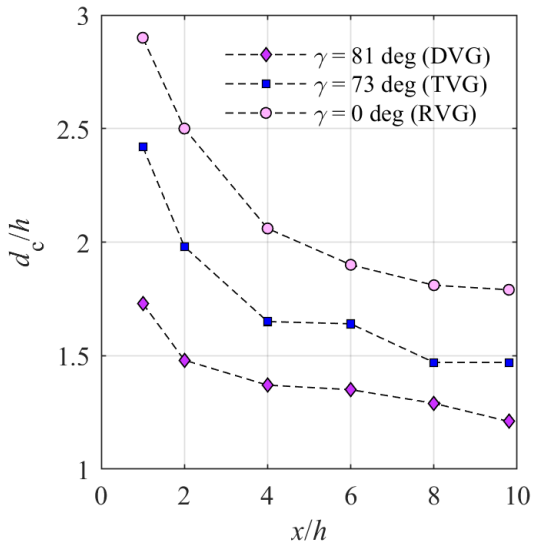

(b)

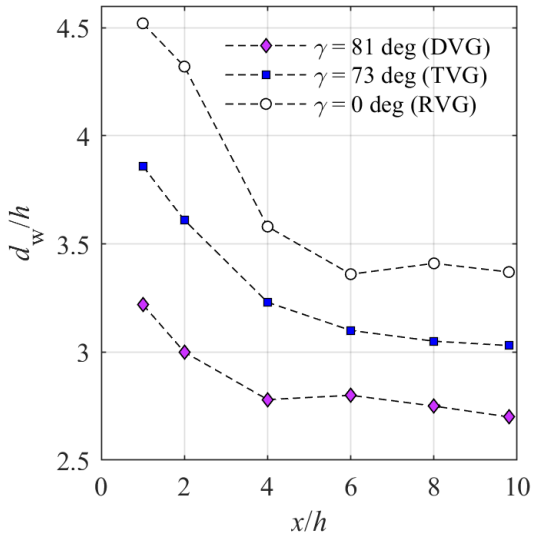

(c)

Fig. 6 (a)The distance between vortex cores (d_c) and (b) the width of wake (d_w) along the wake centerline for the VG with different γ.

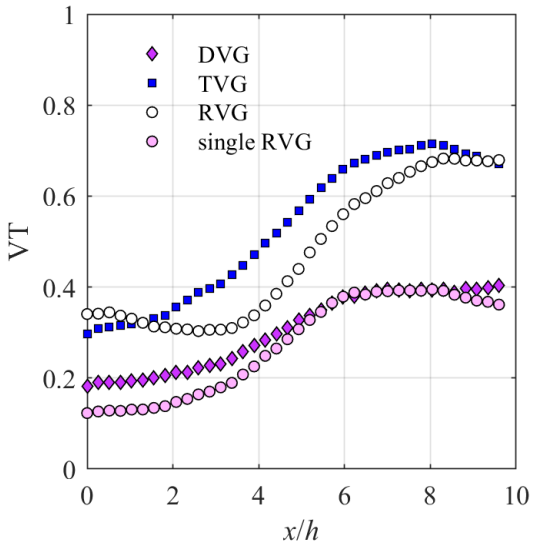

Fig. 7 The rate of vertical transport (VT) along wake centerline estimated using Equation 1.

3.1.2 Momentum transport

To quantitatively evaluate the performance of the VGs, the momentum transport (MT) is estimated by integrating wall-normal transport of streamwise momentum as

$$\mathrm{MT} = \frac{1}{U_\infty^2}\int_{-3h}^{3h}\int_{0.3h}^{2.5h}|\langle UV\rangle|\,\mathrm{d}y\mathrm{d}z. \qquad (2)$$

This equation evaluates the total rate of momentum transport in y direction by integrating the absolute value of $<UV>$ over the y-z plane. The result is plotted along the centerline in Fig. 8. In general, the RVG has the highest MT, followed by the TVG, single RVG and DVG. The MT of RVG is ~20% greater than the TVG and is about twice the single RVG and DVG. As the streamwise distance increases, a small decrease in MT is observed for the paired VG configuration, while MT remains relatively constant for the single RVG. Comparing the RVG and single RVG suggests that the addition of a second vane blade significantly improves the wall-normal momentum transport.

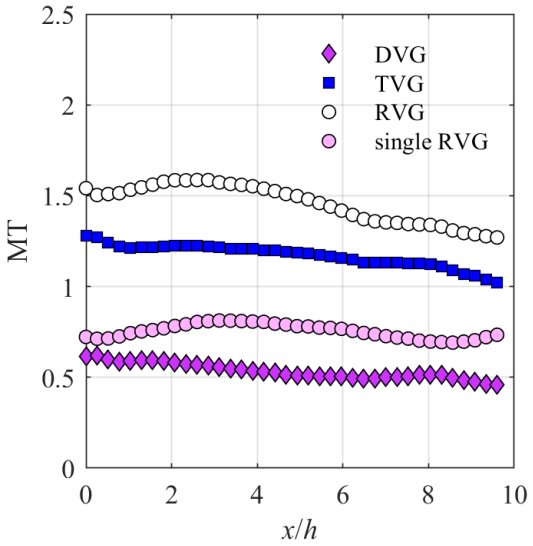

Fig. 8 The wall-normal momentum transport (MT) along the centerline for different VGs.

3.1.3 Drag coefficient

The drag coefficient C_D of each VG is evaluated at $x = 5h$ using the Stereo-PIV measurment. The method of Bohl and Koochesfahani (2009) which accounts for the streamwise velocity fluctuation and downstream pressure deficit is used to estimate the drag coefficient as:

$$C_D = -\frac{2}{c}\iint\left\{\frac{\langle U\rangle}{U_\infty}\left(\frac{\langle U\rangle}{U_\infty} - 1\right) + \varepsilon\left(\frac{\langle U\rangle}{U_\infty} - 1\right) + \left(\frac{u_{rms}}{U_\infty}\right)^2 - \left(\frac{v_{rms}}{U_\infty}\right)^2 + \frac{1}{2}\left(1 - \frac{U_0^2}{U_\infty^2}\right)\right\} dydz. \quad (3)$$

where U_o is the free-stream velocity at the y-z plane of stereo-PIV. The free stream velocity upstream of the VG was indicated by U_∞. The terms u_{rms} and v_{rms} are root-mean-square of velocity fluctuation in x and y directions, respectively. The term $\varepsilon(<U>/U_\infty\text{-}1)$ indicates the variation of free-stream U between the upstream and downstream, and ε is calculated from $0.5\text{-}U_o/U_\infty$. The effect of pressure deficit is represented by the last term, derived from the y-component of Reynolds averaged Navier-Stokes equation, and Bernoulli's equation (Bohl and Koochesfahani 2009). The integration is carried out over a control surface that covers from -3h to 3h, and 0 to 6h in the z and y direction respectively. The calculated C_D is shown in Table 2, along with the wetted area and frontal area of the VGs. The wetted area is defined by the total surface area of VG in contact with fluid.

The largest uncertainty of this estimation comes from the velocity measurement. The uncertainty of the in-plane velocity component σ_V is assumed to be 0.1 pix (Raffel et al. 2018). The uncertainty of the out-of-plane velocity component σ_U is expected to be higher than σ_V due to the stereo-camera arrangement (Prasad and Adrian 1993). In this experiment, σ_U is calculated to be 1.3 times larger than σ_V using

$$\frac{\sigma_U}{\sigma_V} \approx 2\left(\frac{d_o}{S}\right). \quad (4)$$

where d_o is the object distance and S is the distance between the lenses. The uncertainty of C_D is therefore calculated to be 4% using propagation of uncertainty (Ku 1966).

The result shows that the single RVG has the lowest C_D magnitude. The RVG has the largest drag, followed by TVG and DVG. As shown in Fig. 9, a linear ascending trend of C_D is observed with increase of wetted area and frontal area of the VG. The larger drag of RVG and the smaller drag of DVG agree with the observation from Fig. 5; DVG has a smaller wake deficit and RVG has a larger wake deficit.

Table 2 C_D for different VGs at $x = 5h$

VG	Wetted Area (mm^2)	Frontal Area (mm^2)	C_D
DVG	620	116	0.0106
TVG	850	168	0.0142
RVG	1110	220	0.0184
single RVG	555	110	0.0097

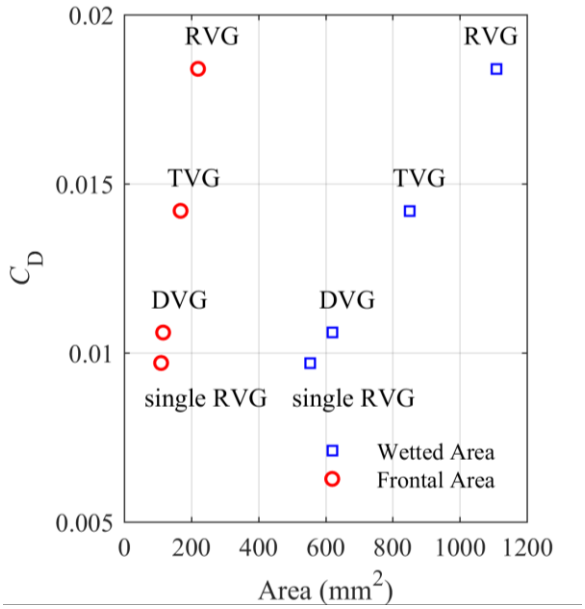

Fig. 9 Estimated C_D against wetted area and frontal area of the VGs. In both cases, C_D increases linearly with area.

3.1.4 Mean vorticity

Iso-surfaces of mean streamwise vorticity, $\langle\Omega_x\rangle$, normalized with U_∞/h, are plotted in Fig. 10. The negative vorticity is rendered in yellow at a threshold of -0.02, and the positive vorticity is shown in red with a threshold of +0.02. The thresholds were selected to visualize both the primary and secondary vortex structures. The mean vorticity was obtained by calculating the velocity gradient using a second order central difference method. In the wake of all VG pairs, two primary counter-rotating vortices are observed. The vortex tubes converge toward each other at the immediate downstream of the VG trailing edge and become parallel further downstream. A pair of weaker secondary counter-rotating vortices is also detected between the primary vortices. This secondary vortex pair rotates in the opposite direction to the primary vortex pair. At the selected vorticity threshold, the iso-surfaces of the secondary vortices only persist for $x < 5h$, while the iso-surfaces of the primary vortices can be clearly observed through the entire measurement domain. The analysis suggests that RVG produces the strongest streamwise vortices, followed by the TVG and the DVG; as γ increases, the steady vortices tend to be weaker. By comparing Figs. 10c and 10d, we conclude that the VG pair configuration slightly increases the vortex strength of both the primary and secondary vortices, in the near wake region as seen by the wider iso-surfaces. Fig. 10 also shows that RVG generates the strongest secondary vortices, which cause the reduction of VT at $h<x<3h$ in Fig. 7.

(a)

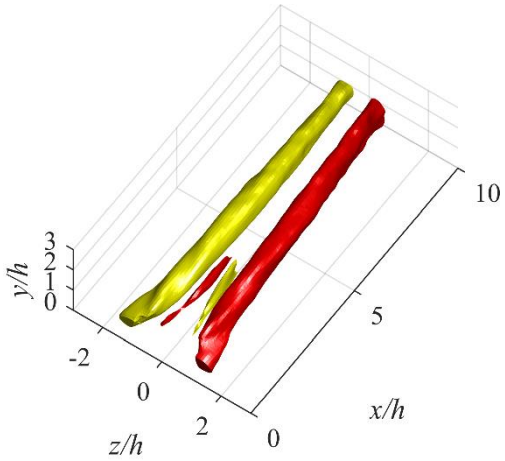

(b)

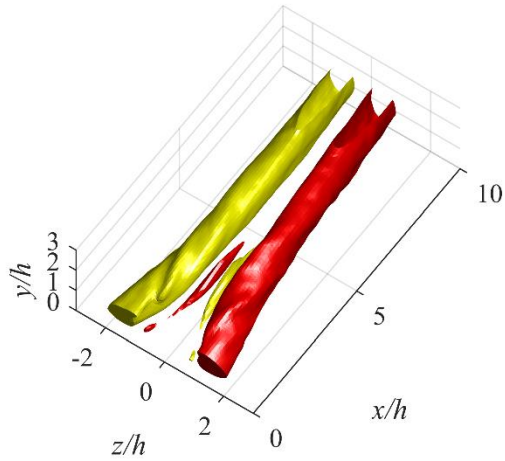

(c)

(d)

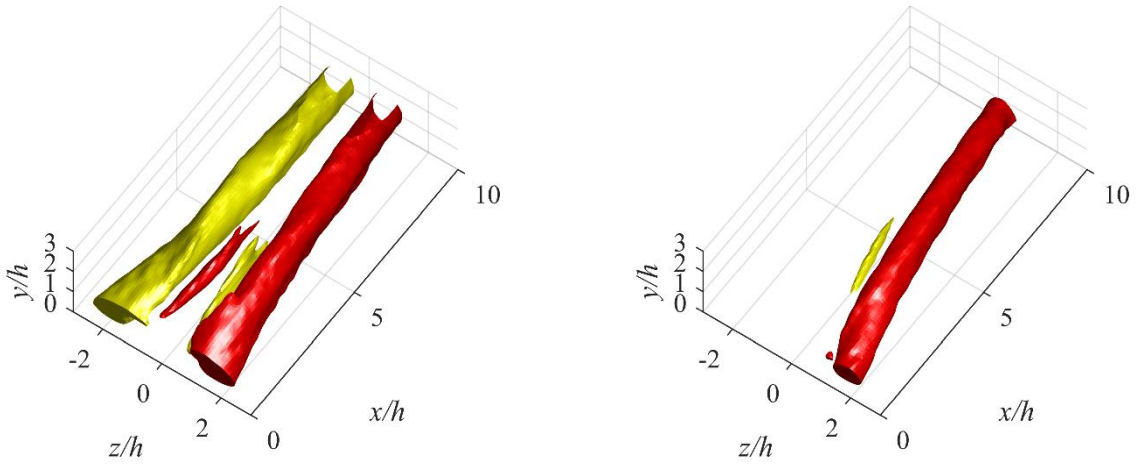

Fig. 10 A visualization of the mean streamwise vorticity, $\langle\Omega_x\rangle$, normalized by U_∞/h in the wake of (a) the DVG, (b) TVG, (c) RVG, and (d) the single RVG. The positive $\langle\Omega_x\rangle$ (clockwise) is colored in red with a threshold of +0.02, while the negative $\langle\Omega_x\rangle$ is presented in yellow at a threshold of -0.02. Primary and secondary streamwise vortices are observed in all the wakes.

3.2 Unsteady velocity field

3.2.1 Vorticity fluctuation

Vorticity fluctuations are investigated here as an indication of the turbulence level. The mean of square of vorticity fluctuation, $\langle\omega_x^2\rangle$, normalized with U_∞^2/h^2 is presented in Fig. 11 with a threshold of 3.5. The spatial derivatives of the fluctuating velocity field are obtained using second-order regression with a kernel of two. The vortices at the immediate downstream of the trailing edge of DVG in Fig. 11a do not contain a significant amount of vorticity fluctuation, indicating their steadiness. At x = ~2.5h, two iso-surfaces appear, become closer, and finally merge. The merged region of high vorticity fluctuation also coincidences with the location of the secondary vortices observed in Fig. 10. For TVG and RVG two regions of strong vorticity fluctuation appear at the immediate downstream of the VG trailing edge and converge at x/h ~3. In general, the largest vorticity fluctuation is generated by the RVG and the weakest by the DVG.

Fig. 11d shows that the single RVG produces a tube of vorticity fluctuation with a relatively large diameter, which is inclined at an angle with respect to the flow direction. The iso-surface maintains its diameter as the streamwise distance increases. Comparison of Figs. 11c and d shows smaller streamwise vorticity fluctuation in the wake of the VG pair. This is associated with increase of steadiness of the counter-rotating vortices since the neighbouring vortex limits the spanwise jitter of the vortices. In case of the single RVG, the vortex has more freedom to move in the spanwise direction, increasing its unsteadiness and vorticity fluctuation as seen in Fig. 11d.

(a) **(b)**

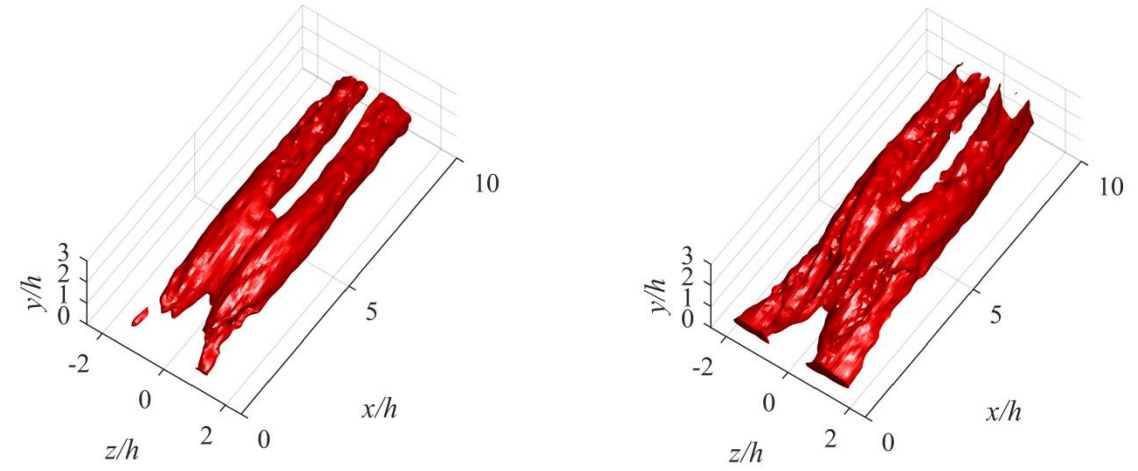

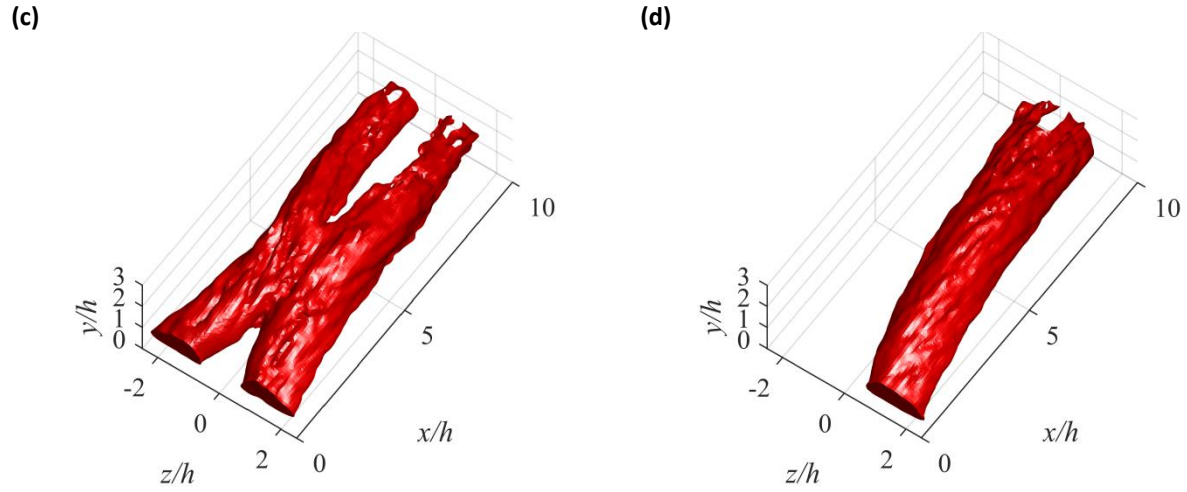

Fig. 11 The time-average of square of the streamwise vorticity fluctuation, $\langle\omega_x^2\rangle$, normalized with U_∞^2/h^2 in the wake of (a) DVG, (b) TVG, (c) RVG, and (d) single RVG. The proximity of the pairs of counter-rotating vortices has a stabilizing effect and reduces the vorticity fluctuations as evident by comparing pair and single RVGs.

3.2.2 Turbulence production

Production of turbulence kinetic energy shows the amount of energy extracted from the mean flow by the VGs. The extracted energy is expected to increase small-scale mixing by turbulence. Production of turbulence, P, is obtained from tomo-PIV based on

$$P = -\Big[\langle u^2\rangle\frac{d\langle U\rangle}{dx} + \langle v^2\rangle\frac{d\langle V\rangle}{dy} + \langle w^2\rangle\frac{d\langle W\rangle}{dz} + \langle uv\rangle\frac{d\langle U\rangle}{dy} + \langle uv\rangle\frac{d\langle V\rangle}{dx} + \langle uw\rangle\frac{d\langle U\rangle}{dz} + \langle uw\rangle\frac{d\langle W\rangle}{dx} + \langle vw\rangle\frac{d\langle V\rangle}{dz} + \langle vw\rangle\frac{d\langle W\rangle}{dy}\Big]. \quad (5)$$

Normalized contour of the turbulence production is presented in Fig. 12 using three different iso-surfaces. The solid red iso-surface represents high production of turbulence, which has a threshold of 0.05. The solid orange iso-surface has a threshold of 0.02, and the transparent yellow iso-surface has a smaller threshold of 0.01. The contour of DVG in Fig. 12a shows that the strongest region of turbulence production lies within x=0-2h, near the trailing edge of the VG. As the streamwise distance increases, the magnitude drops rapidly. The transparent iso-surface of $P/(U_\infty^3 h)$ at 0.01 stays visible until x = 6h in the wake of DVG, while this iso-surface is shorter in the wake of the TVG and RVG. The TVG has the smallest turbulence production. In the wake of RVG, the turbulence production contour is wider and consists of two pairs of cores. The contour of production in Fig. 12d reveals that the single streamwise vortex can extract more kinetic energy from the mean flow than the RVG. The whole streamwise vortex is surrounded by the transparent yellow iso-surface, with two strong turbulence production regions in its core. The difference in pattern between the contours of the pair and single RVG indicates that the conjugate vane-blade has a significant effect in reducing turbulence production within the near wake region. It is also evident that each rectangular vane produces two cores of streamwise vorticity fluctuation due to the leading and trailing edges of the rectangular vane. In general, a reversed trend is observed between turbulence production and the effectiveness of the VG in wall-normal momentum transport. The DVG has a large turbulence production while it is less efficient in wall-normal transport based on the analysis of MT in Fig. 8.

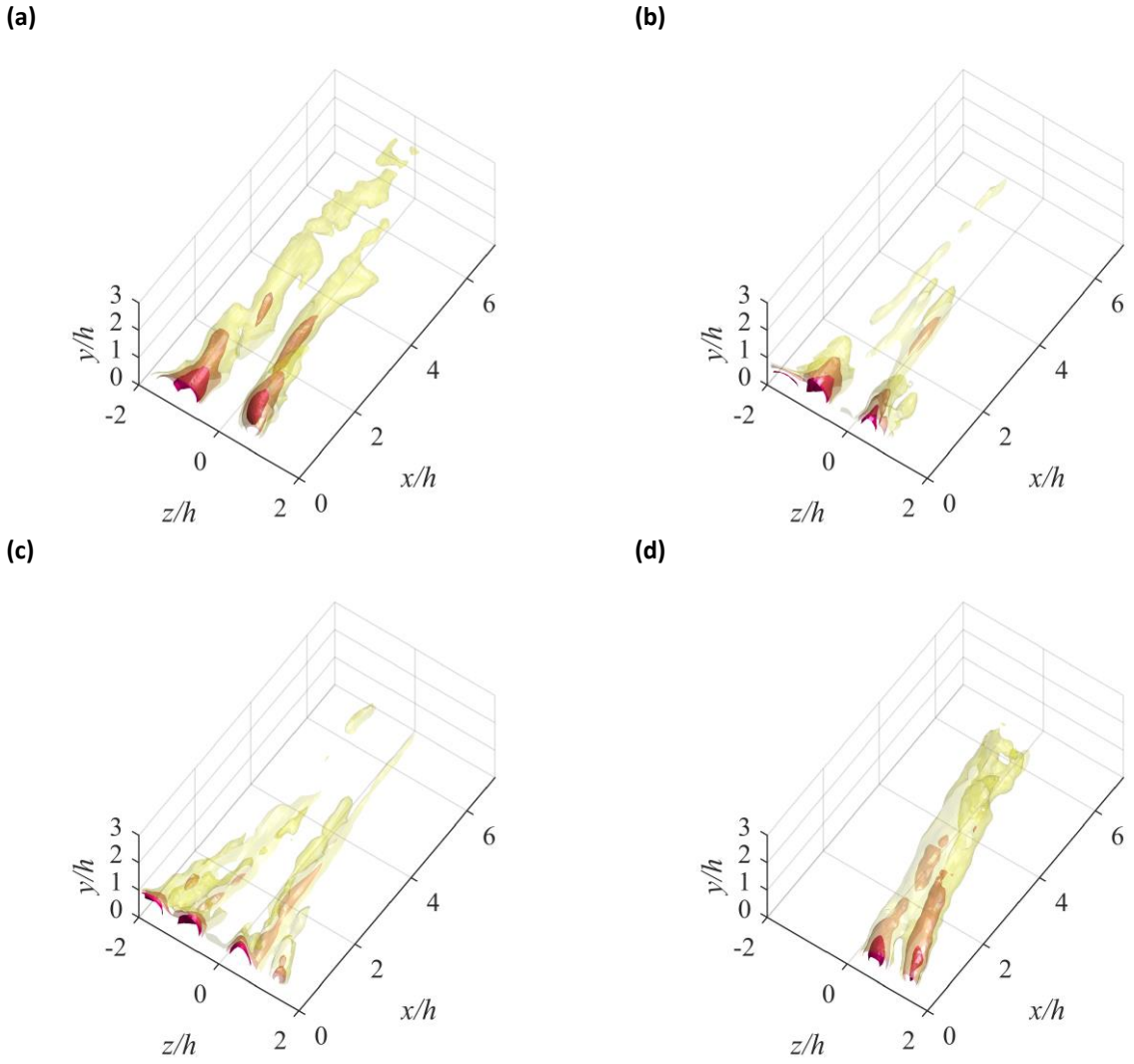

Fig. 12 Iso-surfaces of normalized turbulence production $\langle P \rangle/(U_\infty^3 h)$ in the wake of (a) DVG, (b) TVG, (c) RVG, and (d) single RVG. Three levels of thresholds are selected to represent the intensity variation. The red, orange, and yellow iso-surfaces have thresholds of 0.05, 0.02, and 0.01, respectively.

3.3 Three-dimensional coherent structures

The three-dimensional coherent structures of the wake are investigated through proper-orthogonal-decomposition (POD) based on the snapshot method (Lumeley 1967; Sirovich 1987). The time-resolved three-dimensional fluctuating velocity field was used in the POD analysis to identify the dominant structures and reconstruct a low-order model. As seen in Fig. 13a, the first POD mode of RVG has the largest energy percentage of ~23% while the energy of the first mode of the single RVG is 8%. The larger energy of the first POD modes of RVG indicates a higher degree of coherence and fewer small-scale structures in its wake. The energy of the first POD mode for the other two VGs is much smaller compared with the rectangular vanes. The larger energy of the first POD mode indicates greater coherence of the flow field since few energetic flow structures can reconstruct the instantaneous flow fields. If the energy of the first mode is small, more modes are required to form an instantaneous flow field, which reduces the coherency of the field.

It is also observed that the distribution of POD mode energy is relatively uniform for all the swept VGs (i.e. DVG and TVG). The cumulative energy of the POD modes is also presented in Fig. 13b. TVG and DVG have a similar energy distribution.

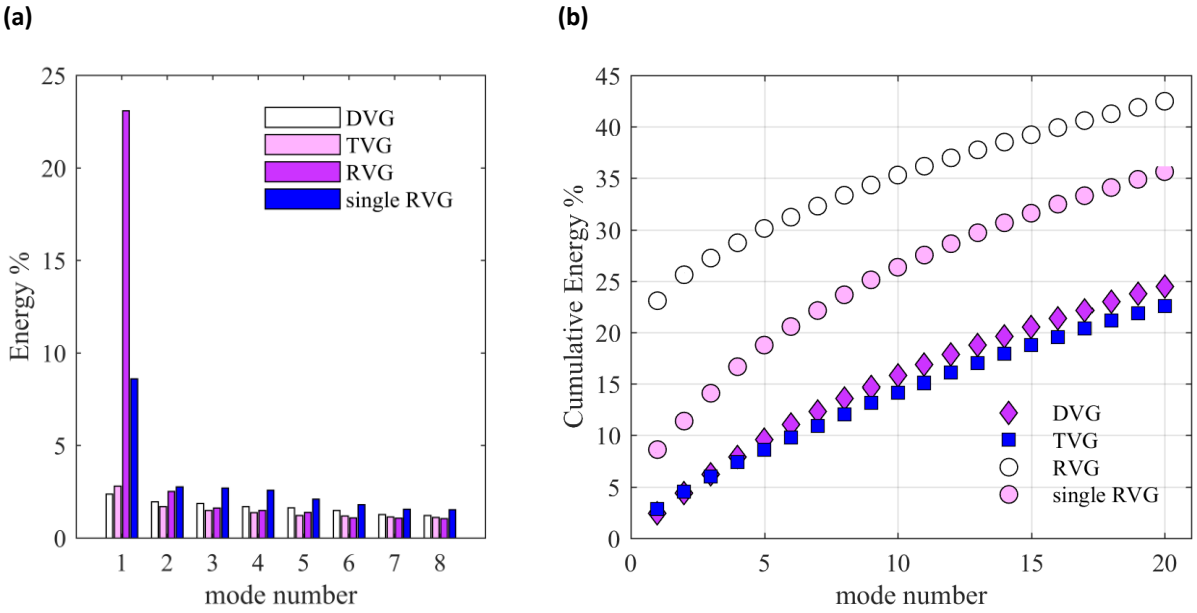

Fig. 13 (a) Distribution of the energy of the POD modes and (b) their cumulative energy for all VGs based on the fluctuating velocity field from tomo-PIV.

The spatial organization of the first POD mode of the VGs is illustrated in Fig. 14 using *Q*-criterion at a threshold of 0.5 s^{-1} (Hunt 1998). The visualization shows that the first mode of DVG and TVG, which only has 2-3% of the total turbulence kinetic energy, is formed of a large number of small-scale structures. The first mode of these two VGs appears as a sheet of discrete vortices. This organization contributes to weakening of the primary streamwise vortices and indicates small-scale mixing in the wake of DVG and TVG. However, the first mode of RVG, with 23% of the total energy, consists of two small streamwise vortices, which follow the pattern of the primary vortices of the mean flow field. This indicates steadiness and the major role of the streamwise vortices in the wake of the RVG. The first POD mode of the single RVG, in Fig. 14d, has two adjacent streamwise vortices along the region where the primary streamwise vortex is located. The double pattern is associated with the movement of the primary streamwise vortex.

When associating the spatial organization with the POD modes, it is observed that the first POD mode of RVG has higher energy and generates a more coherent vortex pattern in the shape of streamwise vortices. Fig. 14 also reveals that the VGs with a flat mode energy distribution tend to have a more distributed vortex pattern with small-scale structures. This was observed to be less effective in transporting momentum in the wall-normal direction.

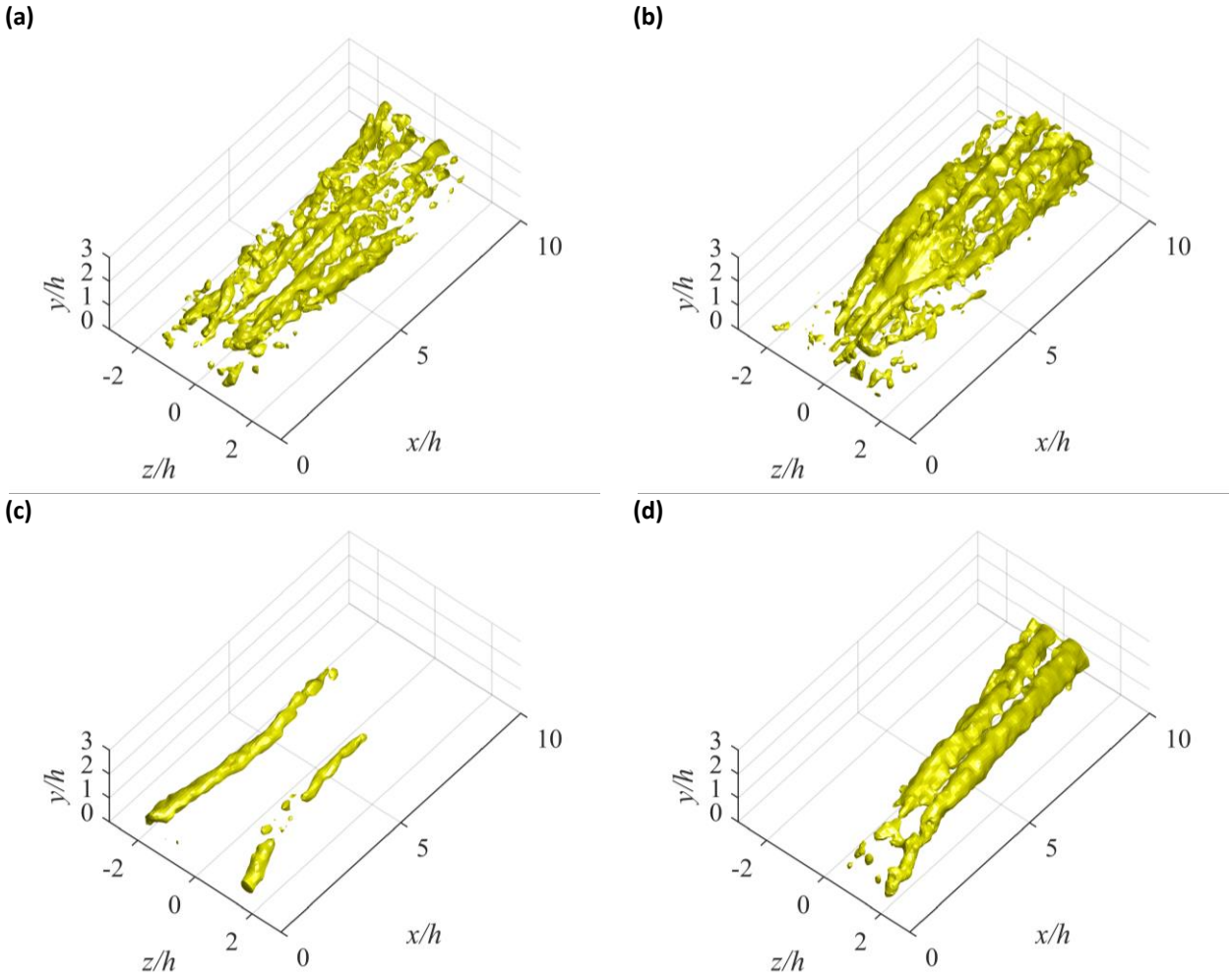

Fig. 14 Visualization of the first POD mode using *Q*-criterion at a threshold of 0.5 s^{-1} in the wake of (a) DVG, (b) TVG, (c) RVG, and (d) single RVG.

To visualize the dominant instantaneous turbulent structures within the wake region, a reduced-order model is generated using the mean flow field and the initial modes that contribute to 40% of the total turbulent kinetic energy. This energy level was selected to eliminate small-scale turbulence and noise, with minimum change to the coherent turbulent structures. The reconstruction for DVG and TVG requires 48 and 56 modes, respectively. For pair RVG only 16 POD modes and for single RVG 26 POD modes are required.

The dominant vortex structures in the wakes of the VGs are presented in Fig. 15 with yellow iso-surface based on *Q*-criterion. The instantaneous wall-normal velocities are also presented to illustrate the transport of momentum and direction of rotation of the vortices. Positive instantaneous wall-normal velocity is colored using transparent green (+0.04 m/s), and the negative instantaneous wall-normal velocity is shown in transparent blue (-0.02 m/s). The primary turbulent structure is observed to be a pair of streamwise counter-rotating vortices for all VGs.

DVG produces a large number of small secondary vortices near the wake centerline as seen in Fig. 15a. A better view is presented in the animation (Online Resource 1); numerous small-scale vortices are observed around the primary vortices even when the flow field is reconstructed using only 40% of the turbulent kinetic energy. There are also small scale spanwise vortices with a tendency to arch over the wake centerline (see the visualization at 340 ms of Online Resource 1).

The reconstructed model of the instantaneous wake of the TVG is presented in Fig. 15b. Two coherent counter-rotating streamwise vortices, and smaller secondary vortices are observed in the animation (Online Resource 2). Based on visual inspection, the primary vortices of TVG are stronger than DVG.

The wake of the RVG is illustrated in Fig. 15c. The primary vortices are more coherent and steady. The secondary vortices are quasi-streamwise vortices with a considerable wall-normal component. The animation (Online Resource 3) demonstrates that the secondary vortices stay visible till x = ~5h. The RVG produces the most coherent, and the strongest primary vortices compared with DVG and TVG. The vortex iso-surface is smooth and has small jitter. The iso-surfaces of the wall-normal velocity also indicates that the wall-normal flow transport is stronger compared to the other VGs.

As shown in Fig. 15d, both primary and secondary vortices are present in the wake of the single RVG. The animation (Online Resource 4) shows that the secondary vortices are partial arches with a strong spanwise component; they are observed after x = 6h. As they move downstream, they tend to grow in spanwise direction, and occasionally connect to the primary vortex, form a full arch. The contour of the wall-normal velocities also suggests that the upward flow transport is stronger than the downward transport. This is associated with the focus ejection motions induced by half-arch vortices. The difference between the contours of the paired RVG and the single RVG reveals that the counter-rotating pair configuration weakens the secondary vortices.

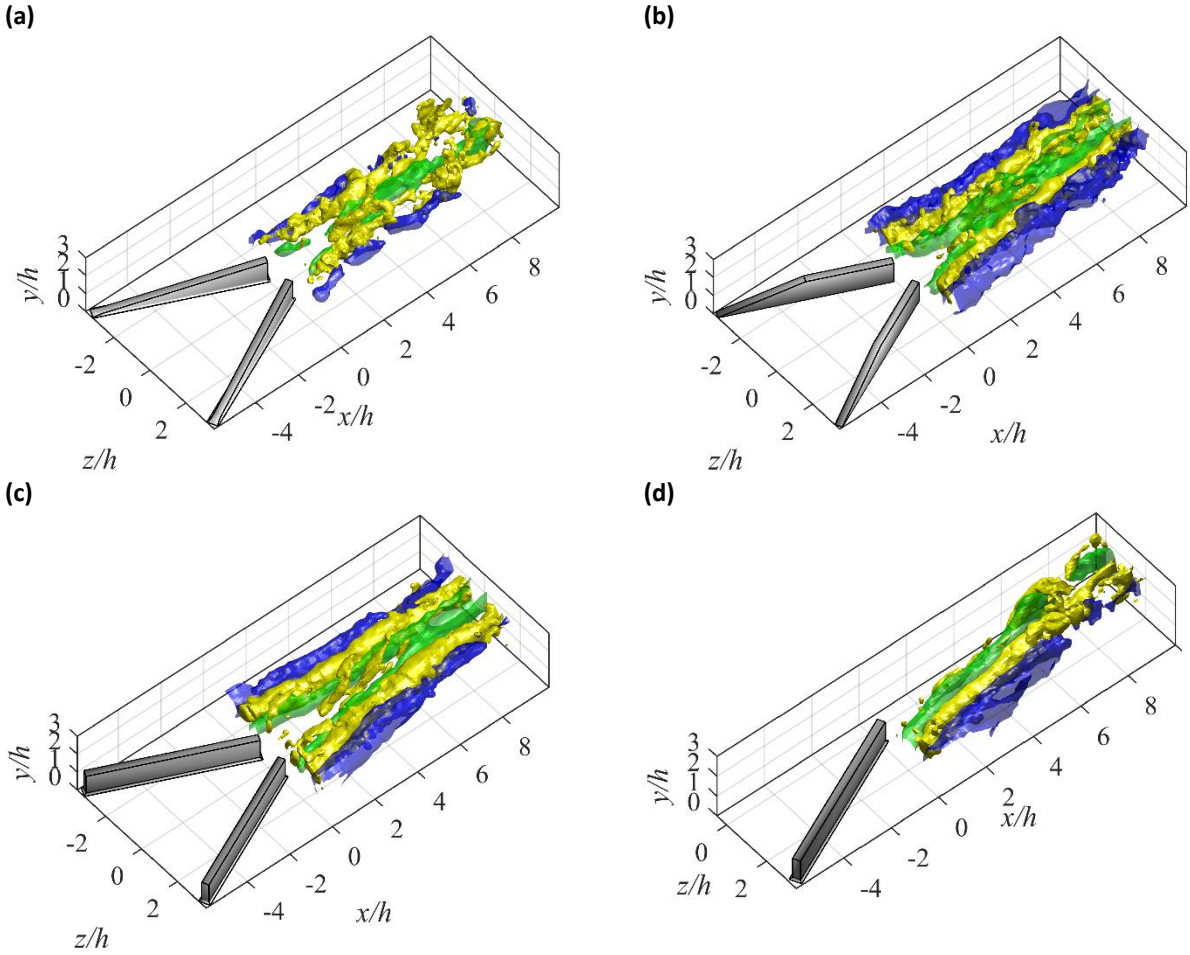

Fig. 15 Low-order reconstruction of instantaneous coherent structures using the mean flow and 40% of total turbulence kinetic energy from POD modes. Q-criterion at 80 s^{-2} (yellow), and wall-normal velocity at V = 0.04 m/s (green) and V = -0.02 m/s (blue) are shown in the wake of (a) DVG, (b) TVG, (c) RVG, and (d) single RVG.

4 Overall performance

The performance of the VGs is evaluated here based on wall-normal momentum transport and drag. An effectiveness parameter, *e*, is defined to evaluate momentum transport at the expense of drag following

$$e = \frac{\int_0^{5h} \mathrm{MT} \mathrm{d}x}{c_\mathrm{D}}. \quad (6)$$

This parameter allows comparison of VG performance per unit of parasitic drag. As seen in Table 3, TVG has the largest *e*, showing best performance in terms of wall-normal transport while producing the lowest drag. The RVG also has a similar performance with about ~2% difference relative to TVG. The single RVG is not as effective as paired RVG, but it is still more effective than the DVG. Therefore, TVG has the best performance in terms of mixing per unit drag, followed by RVG and single RVG. In applications that the device drag is not critical, RVG provides larger mixing relative to other VGs with the same height. The analysis also shows that the sweep angle of TVG increases the VG performance; however, the larger sweep angle of DVG reduces the performance.

Table 3 Comparison of VG performance.

VG	γ (deg)	$\int MT\mathrm{d}x$	$e\times10^{-2}$
DVG	81	2.8	2.5
TVG	73	6.1	4.4
RVG	0	7.8	4.3
single RVG	0	3.9	4.0

5 Conclusion

An experimental investigation of the wake of three vortex generators (VGs) with different vane shapes was carried out using time-resolved tomographic particle image velocimetry (tomo-PIV) and stereoscopic PIV (stereo-PIV). The VGs include delta, trapezoidal and rectangular shape vanes in a paired configuration indicated as DVG, TVG, and RVG. The leading-edge sweep angle of the vane varies from a large to a small value for DVG, TVG, and RVG, respectively. A single VG with rectangular vane was also investigated to evaluate the effect of vane pairing.

The results showed that there are two counter-rotating streamwise vortices in the wake of all the paired VGs. The counter-rotating vortices are the key element in flow mixing and induce a focused motion away from the wall at the centerline of the wake, surrounded by two streamwise regions with downward motions towards the wall. A pair of secondary counter-rotating streamwise vortices was also observed.

The wake of RVG had the strongest wall-normal motion, extended over a longer streamwise extent. The second strongest wall-normal mixing is induced by TVG, followed by DVG. In general, the increase of leading-edge sweep angle weakens the primary vortices, and therefore reduces the wall-normal flow transport.

The distance between the two primary streamwise vortices increased with reduction of the sweep angle of the vane. Therefore, the RVG had the widest wake region and DVG had the smallest wake region. The estimation of drag based on momentum deficit also showed that RVG had the largest drag, while TVG and DVG had 24% and 42% less drag, respectively.

The single RVG had a larger streamwise vorticity fluctuation and turbulence production relative to the pair RVG. This is associated with the stabilizing effect of the neighbouring counter-rotating vortices.

The DVG had the largest turbulence production, which indicates that more kinetic energy of the mean flow is extracted by small-scale vortices. This suggests less efficient mixing by small-scale vortices as opposed to the more efficient mixing by the quasi-steady streamwise vortices. The distribution of the energy of the POD modes also shows a uniform distribution of energy for the DVG and TVG. The first POD mode of DVG and RVG only have 2-3% of the total energy, while RVG contains about 23% of the energy in two counter-rotating streamwise vortices. Therefore, the wake of RVG consists of more coherent streamwise vortices, which are significantly more effective in wall-normal mixing.

The study shows that a rectangular vane is more effective in inducing steady streamwise vortices relative to trapezoidal and delta shape vanes. However, the evaluation of the wall-normal momentum transport per unit of drag indicates that TVG has the best performance. The results point out the potential of further increasing the VG effectiveness by adjusting the sweep angle γ. Nevertheless, the DVG presents the worst performance, which suggests that the sweep angle should be carefully selected to maintain the effectiveness in momentum transport while producing minimum drag.

References

Betterton J, Hackett K, Ashill P, Wilson M, Woodcock I (2000) Laser doppler anemometry investigation on sub

boundary layer vortex generators for flow control. 10th International Symposium on Applications of Laser Techniques to Fluid Mechanics 10–13

Bohl DG, Koochesfahani MM (2009) MTV measurements of the vortical field in the wake of an airfoil oscillating at high reduced frequency. J Fluid Mech 620: 63-88

Elsinga GE, Scarano F, Wieneke B, van Oudheusden B. W (2006) Tomographic particle image velocimetry. Exp Fluids. 41(6): 933-947

Forster KJ, White TR (2014) Numerical investigation into vortex generators on heavily cambered wings. AIAA J 52(5): 1059-1071

Godard G, Stanislas M (2006) Control of a decelerating boundary layer. Part 1: Optimization of passive vortex generators. Aerospace Science and Technology 10(3): 181-191

Holmes AE, Hickey PK, Murphy WR, Hilton DA (1987) The application of sub-boundary layer vortex generators to reduce canopy Mach rumble interior noise on the Gulf-stream III. AIAA 25th Aerospace Sciences Meeting, Reno, NL, January 12-15

Hunt JCR, Wray AA, Moin P (1998) Eddies, stream, and convergence zones in turbulent flows Center for Turbulence, Research Report CTR-S88: 193–208

Ku HH (1966) Notes on the use of propagation of error formulas. Journal of Research of the National Bureau of Standards, 70(4): 263-273

Kuethe AM (1972) Effect of streamwise vortices on wake properties associated with sound generation. Journal of Aircraft 9(10): 715-719

Lin JC (1999) Control of turbulent boundary-layer separation using micro-vortex generators. 30th Fluid Dynamics Conference

Lin JC, Howard FG, Selby GV (1990) Investigation of several passive and active methods for turbulent flow separation control. 21st Fluid Dynamics, Plasma Dynamics and Lasers Conference

Lin JC, Howard FG, Selby GV (1991) Exploratory study of vortex-generating devices for turbulent flow separation control. 29th Aerospace Sciences Meeting, Aerospace Sciences Meetings, January

Lin JC, Robinson SK, McGhee RJ, Valarezo WO (1994) Separation control on high-lift airfoils via micro-vortex generators. Journal of Aircraft 31(6): 1317-1323

Lumley JL (1967) The structure of inhomogeneous turbulent flows. Atmospheric Turbulence and Radio Wave Propagation 166-178

Pauley WR, Eaton JK (1994) The effect of embedded longitudinal vortex arrays on turbulent boundary layer heat transfer. Journal of Heat Transfer 116(4): 871-879

Prasad AK, Adrian RJ (1993) Stereoscopic particle image velocimetry applied to liquid flows. Exp in Fluids 15(1): 49-60

Raffel M, Willert CE, Scarano F, Kähler CJ, Wereley ST, Kompenhans J (2018) Particle image velocimetry: a practical guide. Springer, Berlin

Rao D, Kariya T (1988) Boundary-layer submerged vortex generators for separation control - An exploratory study. 1st National Fluid Dynamics Conference, Reston, Virigina: American Institute of Aeronautics and Astronautics

Scarano F, Poelma C (2009) Three-dimensional vorticity patterns of cylinder wakes. Exp Fluids 47(1): 69

Schubauer GB, Spangenberg WG (1960) Forced mixing in boundary layers. J Fluid Mech 8(1): 10-32

Sirovich L (1987) Turbulence and the dynamics of coherent structures. I. Coherent structures. Quarterly of Applied Mathematics 45(3): 561-571

Sun Z (2015) Micro-vortex generators for boundary layer control: principles and applications. International Journal of Flow Control 7(1-2)

Taylor HD (1947) The elimination of diffuser separation by vortex generators. United Aircraft Corporation, East Hartford, CT, Technical Report No 4012: 3

Wieneke, B. (2005). Stereo-PIV using self-calibration on particle images. Experiments in fluids, 39(2), 267-280.

Wieneke B (2008) Volume self-calibration for 3D particle image velocimetry. Exp Fluids 45(4): 549-556

Westerweel J, Scarano F (2005) Universal outlier detection for PIV data. Exp Fluids 39(6): 1096-1100